

Anthropomorphic Low-Inertia High-Stiffness Manipulator for High-Speed Safe Interaction

Yong-Jae Kim 

Abstract—In this paper, a manipulator is proposed for safe human–robot interaction at high speed. The manipulator has both low mass and inertia and high stiffness and strength. It is basically a cable-driven manipulator; nevertheless, by using a unique lightweight tension-amplification mechanism, the manipulator retains high stiffness and strength. The joint stiffness, which is strongly related to the motion control performance, is amplified by the quadratic order. Both 1-degree of freedom (DOF) and 3-DOF joint mechanisms using the tension-amplification mechanism are presented and combined to develop a 7-DOF anthropomorphic manipulator named LIMS. The mass and inertia beyond the shoulder were 2.24 kg and 0.599 kg·m², respectively, which are lower than those of a human. The stiffness of the developed elbow joint was 1410 N·m/rad, which is approximately seven times higher than that of a human. Considering the ratio of stiffness to inertia, the manipulator is expected to show a control performance that is comparable to those of conventional industrial manipulators. Comprehensive experiments, including joint stiffness tests and high-speed interaction tests, were conducted to verify the feasibility of the developed manipulator.

Index Terms—Anthropomorphic manipulator, human–robot interaction, safe robots, tension-amplification mechanism.

I. INTRODUCTION

P HYSICAL human–robot interaction has recently attracted significant attention because it is a key feature that pushes the boundaries of conventional industrial robotics. In the past several years, many industrial robots have been introduced in the market. They include the Baxter and Sawyer robots of re-think robotics, the LeichtBauRoter intelligent industrial work assistant (iiwa) of Kuka, and the universal robot (UR) series of universal robots. These robots were developed to provide safe interactions when making contact or colliding with humans. They are the results of several decades of studies to develop safe human–robot interactions through a range of means, from introducing force or torque sensors to conventional industrial robots to mimicking human anatomy and biological mechanisms.

To detect external force and collisions by using sensors, various types of manipulators with joint torque sensors or

Manuscript received November 5, 2016; revised June 13, 2017; accepted July 10, 2017. Date of publication August 25, 2017; date of current version December 14, 2017. This paper was recommended for publication by Associate Editor I.-M. Chen and Editor P. Soueres upon evaluation of the reviewers' comments. This work was supported by the Koreatech Research Project.

The author is with Korea University of Technology and Education, Cheonan 330-708, South Korea (e-mail: yongjae@koreatech.ac.kr).

This paper has supplementary downloadable material available at <http://ieeexplore.ieee.org>.

Color versions of one or more of the figures in this paper are available online at <http://ieeexplore.ieee.org>.

Digital Object Identifier 10.1109/TRO.2017.2732354

force–torque sensors have been developed. For instance, the lightweight robot (LWR) III of Deutsches Zentrum für Luft-und Raumfahrt is equipped with integrated joint torque sensors and, thus, shows excellent force control characteristics on account of its precise sensors and accurate modeling [1]. However, its mechanical properties are more similar to those of industrial robots than to human arms. Therefore, prevention of collisions and impacts is achieved with exhaustive feedback control under a relatively low speed. This is because the control algorithm is effective for frequencies that are below the closed-loop bandwidth of the system [2].

To ensure inherent safety, mechanically compliant manipulators have been investigated. One of the most widely applied approaches is the series elastic actuator (SEA), which has a constant spring between its actuator output and robotic link [3], [4]. Owing to the inherent safety introduced by intentionally added springs, the SEA systems have been widely applied not only to robots, but also to rehabilitation systems [5]. Along with SEA, the combinations of active and passive components, such as the series–parallel elastic actuator and series damper actuator, have also been investigated [6], [7]. At the expense of safety, SEA has limited position control performance caused by significantly low bandwidth, which, in theory, can be improved by increasing the feedback control gain. Nonetheless, it is difficult to achieve because of the actuator saturation and limited control speed.

To overcome the drawbacks of SEAs, manipulators with variable stiffness joints have been widely investigated in recent years [8]–[11]. This adjustable stiffness capability enables both the safety of SEA and the control performance of conventional rigid joints. However, safety and performance cannot be simultaneously achieved; moreover, the stiffness-adjusting mechanisms increase the mechanical complexity and corresponding mass, which undermines the human-like inherent safety.

A lightweight design with high back-drivability can be considered the ultimate approach to human-like manipulators. The lightweight mechanism guarantees safety at high speeds because the stored kinetic energy is as low as in humans. In a strict sense, the rotational inertia of the links, including the reflected motor and gear inertia, rather than mass must be considered for storing kinetic energy of the rotational joint.

The cable transmission mechanism is suitable for reducing the inertia by placing heavy actuators at the proximal part [12], [13]. Moreover, the cable can be used as a reduction mechanism with negligible backlash and low friction. The WAM arm [14] is one of the most successful commercialized cable-driven manipulators. The weight of the arm beyond the shoulder is 5.8 kg

(a seven degrees-of-freedom (DOF) arm, not including the hand) [15]. It is heavier than the average human's hand/arm weight of 4.5 kg; however, it is significantly lighter than that of the industrial robot of more than 20 kg.

Nevertheless, the low cable stiffness in many cable-driven manipulators can lead to low control bandwidth, and the low cable strength decreases the maximum payload. Furthermore, placing all actuators (i.e., seven actuators for a human-like arm) at the proximal part and transmitting the motions to the distal joints make the mechanism extremely complicated. Moreover, the extended cable length worsens the low stiffness problem.

Many research efforts have focused on decoupling the actuator inertia and output link inertia. Clutch mechanisms that separate the actuator from the output link under excessive output force [16] guarantee safety in emergency situations. Gravity compensation mechanisms are also an effective way to limit excessive force at low speed [17]. Meanwhile, more challenging approaches using antagonistic magnetorheological clutches were introduced, whereby one actuator is located at the base and multiple joints share the actuator torque [18], [19]. Efforts to improve the low-bandwidth drawback of the SEA have also been undertaken [20]. By combining high-torque SEAs—whose heavy actuators are at the proximal part or in the body—and fast and small motors that are directly connected to the joints, large controllable bandwidth and high payload were achieved.

Despite the above achievements, constituting a 6- or 7-DOF manipulators with minimized inertia, such as in a human, are difficult to accomplish because the related concepts are effective at enabling limited DOF. The present author believes that the human-like configuration with high DOF is one of the most important features for interhuman-level interactions. This is because it satisfies not only aesthetic factors in interactions, but it also provides actual usefulness as a versatile cooperation partner.

It is well recognized that safety is of paramount importance in human–robot interactions. Therefore, most of the aforementioned robots have moderately slow motion, while the interaction between human is performed in a significantly higher speed range. To enhance the capability of human–robot interactions to an “interhuman interaction” level, collisions, or impacts should be treated not only as an object to be absorbed or mitigated, but also as a means for communication and cooperation. Therefore, the high-speed interaction capability that harnesses the collision and impact can be considered an important factor for interhuman-level interactions.

This paper presents a 7-DOF manipulator referred to as a low inertia manipulator with high stiffness and strength (LIMS). It is depicted in Fig. 1. It satisfies both the control performance and safety needs at high speed. All seven motors are mounted at the shoulder part. Steel wires transmit the motor motions to the elbow and the wrist at the distal part, which is similar to conventional cable-driven manipulators. However, a unique lightweight tension-amplification mechanism retains the joint stiffness in the quadratic order without increasing mass and inertia. The mass beyond the shoulder is only 2.24 kg. Nevertheless, the stiffness and strength are comparable to those of industrial robots. The basic concept and joint mechanism were introduced in [21]. In this paper, detailed explanations of the improved hardware, including the wire routing and shoulder

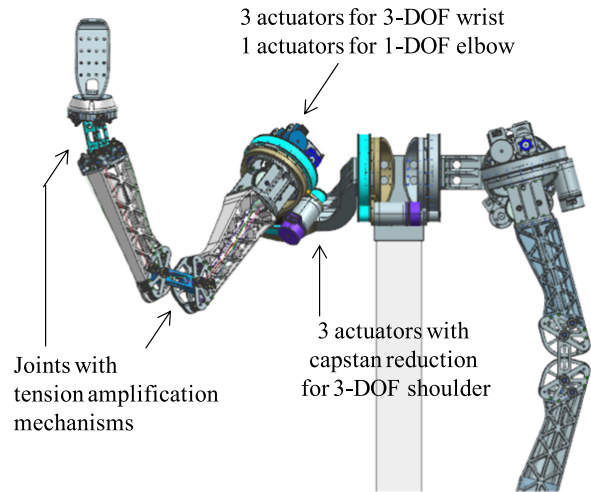


Fig. 1. Proposed LIMS.

actuation mechanisms, are presented. A thorough analysis and experimental verification of the inertia, stiffness, repeatability, payload, and high-speed contact were conducted.

The remainder of this paper is structured as follows. In Section II, safety and performance metrics at high speeds are considered and the design philosophy is introduced. Section III describes the basic mechanics of tension amplification and the detailed mechanical design of the proposed manipulator, LIMS. In Section IV, a stiffness and strength analysis of LIMS is presented. Section V verifies the safety and control performance characteristics of LIMS by thorough experiments. Section VI concludes this paper.

II. SAFETY AND PERFORMANCE AT HIGH SPEED

A. Safety at High Speed

In terms of safety during interaction, conventional robotic arms cannot match human arms. Clapping, hugging, patting, and even gesturing a “high five” are natural and easy with human arms; however, these motions are extremely difficult and dangerous for robotic arms. Various safety metrics in human–robot interactions have been investigated and suggested over several decades. The head injury criterion (HIC) is a well-known and widely used metric. HIC is derived from the average acceleration of a human head and the application time. Other criteria, such as ISO10218, are limited by a maximum speed (0.25 m/s), power (80 W), or force (150 N). Most of these criteria indicate that decreasing the total energy transferred to humans and increasing the transferring time are the most effective ways to reduce injury. Thus, decreasing the total transferring energy by minimizing robot inertia can be considered a fundamental approach to reduce injury and even utilizing impact as communication and collaboration with humans.

Haddadin *et al.* conducted a thorough analysis of safety in human–robot interactions and determined some important facts [22]. One fact is that no significant injury can be observed at a moderate velocity regardless of the robot mass (unconstrained blunt impacts and impact velocity under 2 m/s). This is reasonable because colliding with a massive robot at 2 m/s is intuitively

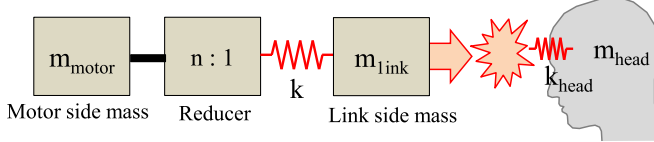


Fig. 2. Simplified model of collision between the robot and human head.

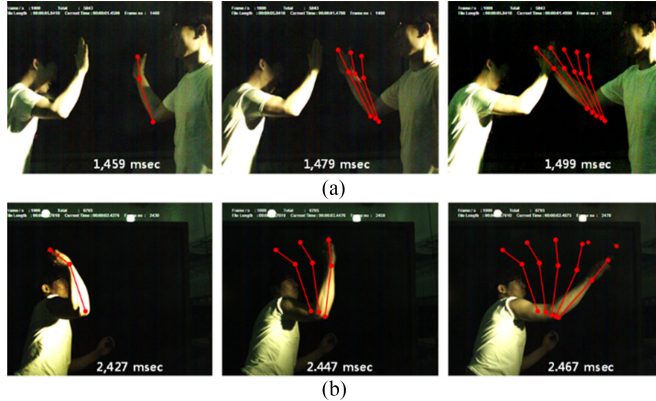


Fig. 3. Snapshots of physical human interactions and motions captured by 1000-frames/s high-speed camera (showed at 20-ms intervals). (a) High-five motion. (b) Throwing motion.

the same as colliding with a wall while walking at 2 m/s. Fig. 2 illustrates a simplified model of the collision between the robot link and the head. Regardless of how large the link mass m_{link} is, the head is not injured on account of the relatively small head mass m_{head} .

Although 2 m/s can be a sufficient speed for safe robot motion, typical interactions between humans are performed in a higher range. To determine the interaction speeds of humans, several motions were captured by a high-speed camera (EoSens MC3011). Fig. 3(a) shows a “high-five” motion. The subject on the right is a 25-year-old 82-kg male. The exerted maximum speed and force do not cause pain or injury. The measured speed of the hand is 7.12 m/s, which is significantly higher than that in human–robot interactions. Fig. 3(b) presents the throwing motion by the same subject, and the speed is 15.6 m/s. The results of these experiments imply that safety should be reconsidered at a higher speed range for human-level interactions.

Fig. 4(a) illustrates the HIC graphs according to the effective mass of the robot. This is similar to the graph in [22]; however, the graphs were calculated at a higher speed range of 1 to 10 m/s. HIC is defined as

$$\text{HIC} = \max_{t_1, t_2} \left\{ (t_2 - t_1) \left(\frac{1}{t_2 - t_1} \int_{t_1}^{t_2} |\ddot{x}_H| dt \right)^{2.5} \right\} \quad (1)$$

where \ddot{x}_H denotes the acceleration of the head expressed in g-force, and t_1 and t_2 are the time intervals within the collision such that $t_2 < t_1$ and $t_2 - t_1 \leq \Delta t_{\text{max}}$. Roughly speaking, HICs of 100 and 1000 mean maximum values of nonlife-threatening and life-threatening injuries to the brain, respectively. In this study, the maximum time duration Δt_{max} was

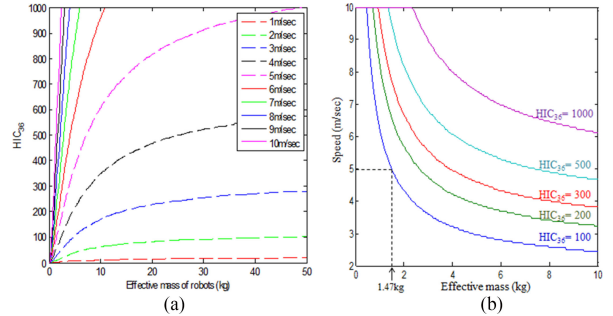


Fig. 4. (a) Relationship between the effective mass and HIC according to speed. (b) Relationship between the effective mass and speed according to the HIC.

set to 32 ms and the mass and stiffness of the head were assumed to be 4.53 kg and 370 N/mm, respectively.

Unlike the results under 2 m/s in [22], the graphs show that HIC values are very closely related with the effective mass. As shown in Fig. 4(a), the HIC value rapidly rises as the speed increases. For instance, the robot with a relatively low effective mass, such as LWR-III with 17 kg [19], has a life-threatening value of 1000 at 5.6 m/s. This speed is not severe in human interaction (HIC = 195 with effective mass of the human arm, 1.998 kg and 5.6 m/s).

Fig. 4(b) shows the speed versus the effective mass graph satisfying several HIC values. To enable the robot to move up to 5 m/s while also satisfying the HIC value of 100, the effective mass should be lower than 1.47 kg. This requirement may be too strict because a direct collision between the head and the robot with no bumpers or soft covers is assumed in this situation. Nevertheless, achieving extremely low effective mass by minimizing the rotational inertia of the robot is still crucial for safety at high speed.

Another unexpected result presented in [22] was that adding more compliance to the joint did not significantly reduce the impact characteristics. This is because the conventional reduction gears for industrial robots, such as harmonic drives, already have sufficient compliance to decouple the effect of the motor inertia. As the motor side inertia is amplified by the quadratic order of the gear ratio, as shown in Fig. 2, the total effective mass is

$$m = m_{\text{link}} + n^2 \cdot m_{\text{motor}}. \quad (2)$$

According to [22], only the link mass m_{link} affected the safety. On the other hand, the amplified motor inertia can arouse unnatural sensations during interactions. If we attempt to shake hands with an industrial robot, we can easily realize the degree to which the exaggerated inertia causes awkward sensations. Consequently, the amplified motor inertia should be considered for improved human–robot interactions. Meanwhile, it can be ignored when considering safety on account of sufficient compliance between the links and actuators.

B. Performance in High Speed

High stiffness and strength are essential properties of the manipulator performance. Especially, stiffness is significantly

related to the controllable speed and tracking performance because the stiffness and the mass determine the system bandwidth. Therefore, we can estimate the controllable speed and tracking performance using the natural frequency, which is approximately proportional to the bandwidth as

$$\omega_n = \sqrt{\frac{k}{m}} \quad (3)$$

where k and m can be the joint stiffness and link inertia, respectively. Alternatively, they can be considered the effective mass and equivalent stiffness of an end effector in Cartesian space. For example, many lightweight cable-driven manipulators tend to have low bandwidths because of the low joint stiffness compared to the link inertia. Even if a cable-driven manipulator has low inertia by placing heavy motors at the proximal end, the system will have poor performance if it has low stiffness caused by the cable. This means that increasing k/m is important. By considering the cable as a spring component, a cable-driven mechanism can be controlled as an SEA and, theoretically, the SEA bandwidth can be increased by increasing the feedback gain. However, in actual cases, the gain is limited by many factors, such as stability, controller speed, motor capacity, etc. Therefore, increasing k/m by increasing stiffness and decreasing mass can remain a valid effort for improved control performance.

The measurement of the stiffness of human joints continues to be contentious issue. Nonetheless, the stiffness of the human elbow joint is reported to be approximately 350 N·m/rad [23], which is low (the joint stiffness of LWR III is approximately 10 000 N·m/rad). However, it is substantially greater than those of other cable-driven manipulators (the joint stiffness in [12] is 35 N·m/rad).

C. Design Philosophy

To develop an inherently safe manipulator without compromising performance, the following design factors are required.

- 1) *Extremely low inertia to minimize stored kinetic energy:* The inertia of the human arm is approximately 0.64 kg·m² [24], while that of most industrial robots such as LWR III is more than 4.5 kg·m². As the inertia is directly proportional to the kinetic energy, the human arm has about seven times less kinetic energy.
- 2) *Extremely low mass:* Conventional industrial robots consume a substantial amount of motor torque to support their own weight. The human arm weighs 4.5 kg, but most industrial robots such as the UR5 of Universal Robots weigh 15 kg or more.
- 3) *High stiffness comparable to that of industrial robots:* As mentioned above, the joint stiffness of industrial robots such as LWRIII is at least 10 000 N·m/rad, while that of a human is 350 N·m. To achieve a dynamic performance comparable to industrial manipulators, the stiffness inertia ratio should be made high by increasing the stiffness.
- 4) *High payload comparable to that of industrial robots:* Human-size robot manipulators have various payloads. For instance, the payload of the dual-arm YuMi robot of ABB Co. is 0.5 kg per arm. However, LWRIII has a 14-kg

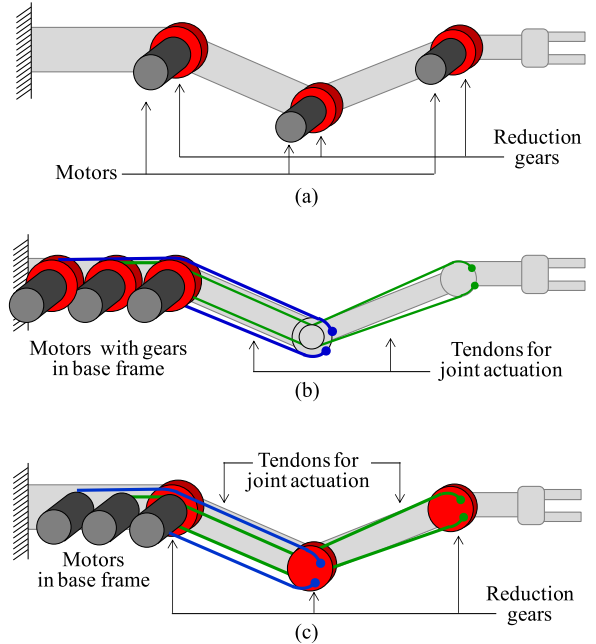


Fig. 5. Conceptual structures of manipulators. (a) Conventional industrial robot. (b) Cable-driven manipulator. (c) Example of a hybrid structure.

payload because huge efforts have been made to minimize its weight and increase joint torque by customizing the harmonic drive gears, making carbon-fiber frames, and other modifications. Despite this diversity, a manipulator must have a sufficiently large payload to install various grippers or robotic hands and to manipulate as many types of objects as possible.

- 5) *Efficiency and back-drivability:* To apply the right amount of energy to the robot, an efficient mechanism with minimal frictional loss is required. Moreover, high back drivability enables the sensing of external forces without expensive force or torque sensors.
- 6) *Sufficient DOF with a human-like configuration without losing or reducing the aforementioned requirements:* The minimum DOF needed to manipulate objects freely in 3-D space is 6. However, for larger workspaces and higher versatility, it is desirable for the manipulator have 7 DOF, as in human arms.

Fig. 5 illustrates the configurations of the motors, gears, and links for several types of manipulators. Fig. 5(a) shows the typical configuration of industrial robots with high inertia and mass on account of the heavy components, such as the motors and gears in the distal part. Fig. 5(b) is a common configuration of a cable-driven manipulator in which the motors and gears are at the proximal part. As previously mentioned, the elasticity and limited strength of the cables causes the low stiffness and low strength of the robot. If high payload wires are used to improve the stiffness and strength, the mechanism will become complicated and bulky because the wires require large-size pulleys, and frames must withstand the high compression caused by the high tension of the wire.

Fig. 5(c) depicts a tradeoff between (a) and (b) and has many advantages over them. Fig. 5(c) has lower mass and lower

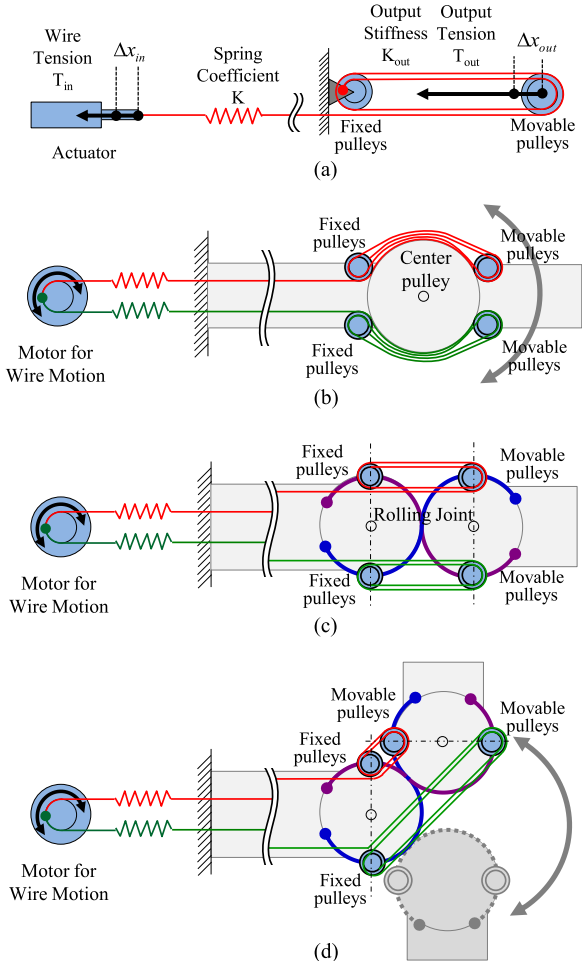


Fig. 6. (a) Basic concept of the tension-amplifying mechanism using a block and tackle mechanism. (b) Revolute joint using the tension-amplification mechanism. (c) and (d) Proposed 1-DOF joint mechanism using the rolling joint.

inertia than (a). Moreover, (c) has higher stiffness than (b), as the stiffness is amplified in the quadratic order, which is explained in the next section. However, the inertia can be still substantial because the heavy gears are situated at the distal part. Moreover, the mechanism can be bulky and complicated because the cable mechanism for multiple DOF joints is difficult to implement. Therefore, a new lightweight transmission and reduction mechanism is required.

III. MECHANICAL DESIGN OF LIMS

A. 1-DOF Tension-Amplification Mechanism

Fig. 6(a) shows the basic concept of a simple tension-amplification mechanism. An actuator on the left side is connected by a cable with a reduction mechanism, which is composed of fixed and movable pulleys. This is the so-called “block and tackle.” If the wire tension exerted by the actuator is \$T_{in}\$, and the number of wires turning around the pulleys is \$n\$ (in Fig. 6(a), \$n = 4\$), the resultant tension \$T_{out}\$ by the tension-amplification mechanism is simply

$$T_{out} = nT_{in} \quad (4)$$

where it is assumed that the friction in this mechanism is negligible. If we consider the reduction of motion, the output motion \$\Delta x_{out}\$ is \$n\$ times smaller than actuator motion \$\Delta x_{in}\$, i.e., \$\Delta x_{out} = \Delta x_{in}/n\$. Therefore, the resultant stiffness of the tension-amplification mechanism is

$$K_{out} = \frac{T_{out}}{\Delta x_{out}} = \frac{nT_{in}}{\Delta x_{in}/n} = n^2 \frac{T_{in}}{\Delta x_{in}} = n^2 K \quad (5)$$

where \$K\$ denotes the spring coefficient of the whole wire and it satisfies \$K = T_{in}/\Delta x_{in}\$. This shows that the mechanism amplifies the tension in the quadratic order. For the revolute motion of a robotic joint, a pair of the tension-amplification mechanism shown in Fig. 6(b) is required to form antagonistic wire motion. The pulley at the center of the joint makes the agonistic and antagonistic wire motions symmetric. Without this pulley, the wire motions will not be symmetrical, which means that an individual motor for each wire is needed. This mechanism has a limited range of motion (ROM) and can cause substantial friction between the pulley and wires.

By adopting a rolling joint, as in Fig. 6(c), the motions of the wire pair become symmetrical, and the ROM can be larger (compare Fig. 6(b) and Fig. 6(c)). The two rolling surfaces have circular shapes, and two additional wires (blue and purple wires in the figure) prevent slipping and enable pure rolling. These two wires for rolling motion can be replaced with the gear teeth for miniaturization, such as surgical instruments. For further details on this application, refer to [24]. As shown in Fig. 6(c) and Fig. 6(d), the two sets of fixed pulleys are placed at points equidistant from the center of the rolling surface of the proximal link, while the set of movable pulleys is placed at points equidistant from that of the distal link. This arrangement of the pulleys allows symmetric wire motion, which is verified in the remaining part of this section. Similar to the basic concept shown in Fig. 6(a) and explained by (4) and (5), this 1-DOF joint mechanism also amplifies the torque and torsional stiffness linearly and quadratically, respectively, as described in detail in Section IV.

The relationship between the wire motion and joint angle can be derived from Fig. 7(a), where the fixed and movable pulleys are omitted for ease of explanation. In this figure, \$l_{left}\$, \$l_{right}\$, \$d\$, \$w\$, and \$\theta\$ denote the total lengths of the agonistic and antagonistic wires wound between the two centers of the pulleys, diameter of the rolling surface, width between the agonistic–antagonistic pulley centers, and the bending angle, respectively. If the joint is in a straight pose (\$\theta = 0\$), \$l_{left}\$ and \$l_{right}\$ have the same length \$nd\$, where the amplification number \$n\$ is the number of wire turns around the pulleys, as previously described. In the case of bending, the two lengths are obtained as

$$l_{left} = n \left(d - w \sin \frac{\theta}{2} \right), \quad l_{right} = n \left(d + w \sin \frac{\theta}{2} \right). \quad (6)$$

If we consider only the amount of change of the left and right wires \$\Delta l_{left}\$ and \$\Delta l_{right}\$

$$\Delta l_{left} = -\Delta l_{right} = nw \sin \frac{\theta}{2}. \quad (7)$$

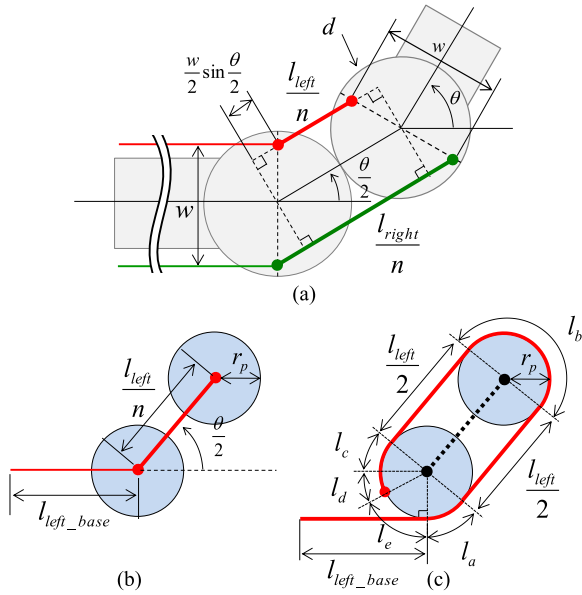


Fig. 7. Relationship between the wire motion and joint angle. (a) Mechanical schematic of the 1-DOF joint. (b) Simplified and (c) actual wire paths, respectively, around the fixed pulleys and movable pulleys.

This equation confirms that the motion of the wire pair is fully symmetrical and simple actuation mechanism with one motor is applicable. Equations (6) and (7) were derived with the simplified model by ignoring the diameter of the fixed and moving pulleys. Fig. 7(b) and Fig. 6(c) illustrates the simplified and actual wire paths, respectively. Assuming an even number of n (here, $n = 2$), the actual wire length is

$$\begin{aligned} l_{total} &= l_{left_base} + l_a + l_{left}/2 + l_b + l_{left}/2 + l_c + l_d \\ &= l_{left_base} + l_{left} + (2\pi r_p - l_e). \end{aligned} \quad (8)$$

When the bending angle θ changes, only the lengths l_a and l_c change accordingly and the others are invariant. Therefore, the actual wire length l_{total} in (8) depends only on l_{left} and the movement of actual wire is exactly the same as (7), which is valid for every even number of n . To sum up, by setting n as an even number, and fixing the wire end on the proximal frame, the actual wire movement agrees with (7).

Fig. 8(a) shows the details of the elbow joint designed and implemented using the proposed 1-DOF tension-amplification mechanism. The flexion wire (red line) and extension wire (green line) come from the motor assembly shown in Fig. 8(d). Each wire goes through a redirection pulley and turns around the fixed and movable pulleys. Note that all the pulleys including the fixed pulleys are freewheeling pulleys with bearings. The ROM of the joint is 180° , and the amplification number n is 6. Because it is comprised of aluminum alloy and 3-D-printed acrylonitrile butadiene styrene (ABS) material without motors or reduction gears, it has a substantially lower mass compared to that of conventional industrial manipulators. The mass and inertia distribution are detailed in Section V. Because (7) and (8) verify that the displacements of the agonistic and antagonistic wires are identical, the length of the total wire path is invariant at any joint angle. Thus, the proposed joint does not require

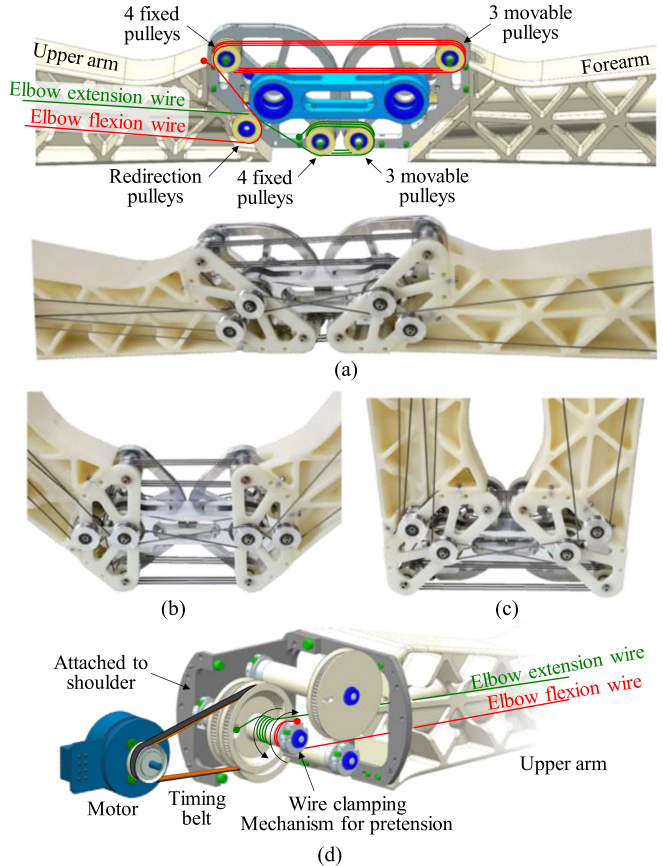


Fig. 8. Detailed design of the elbow joint and its implementation. (a) Straight pose ($\theta = -90^\circ$) with its detailed design. (b) Center of ROM ($\theta = 0^\circ$). (c) Fully bent pose ($\theta = 90^\circ$). (d) Wire clamping mechanism for pretension.

tensioner mechanisms to prevent wire slack. Instead, wire clamping mechanisms that adjust the total wire length to set the pretension were implemented in the motor assembly of the upper arm frame, as shown in Fig. 8(d). The wires are connected to the motor through a timing belt for additional reduction. To prevent slack, the pretension was set to the half of the tension at the maximum payload using the clamping mechanism. Therefore, at the maximum payload, the tension of the pulling wire reaches the maximum tension and that of the loosening wire goes to zero tension but does not cause slack.

B. 2-DOF and 3-DOF Tension-Amplification Mechanism

The 1-DOF tension-amplification mechanism and developed elbow joint were explained in the previous section. For the wrist, the high-DOF joint can be constructed by simply connecting in serial several proposed 1-DOF mechanisms. However, this joint configuration can be unsuitable for dexterous manipulation on account of lack of workspace, and the wire path can be overly complicated. Thus, a new way to extend the proposed concept is needed without sacrificing the tension-amplifying property, wide ROM, simplicity, etc.

Fig. 9(a) illustrates an extended concept of the tension-amplification mechanism. There are two hemispherical rolling surfaces instead of the circular-shaped part that are surrounded

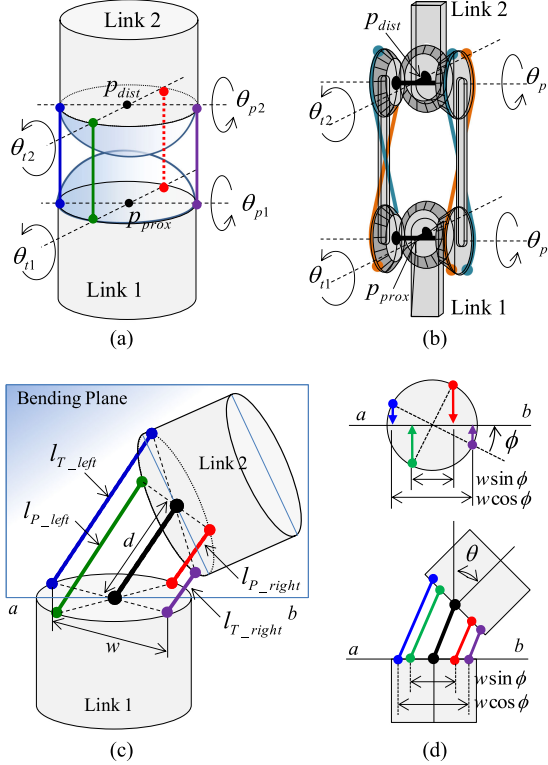


Fig. 9. Conceptual design of 2-DOF tension-amplification mechanism. (a) Ideal model of the 2-DOF rolling joint. (b) Bevel gear set with wire coupling to emulate 2-DOF rolling motion. (c) Mechanical schematic of the 2-DOF rolling joint and (d) its top and front views.

by two wire pairs for the 2-DOF pan-tilt motion. This ideal model is almost infeasible because the hemispheres occupy the wire path when bending and the contact point cannot endure slipping and torsional forces. In addition, it must be verified whether each wire pair exhibits symmetric behavior, even under combined pan-tilt motion.

To emulate the spherical rolling contact, a unique 2-DOF rolling joint is proposed, as shown in Fig. 9(b). It is composed of two identical bevel gear sets. Each bevel gear set is composed of three bevel gears, one center gear, and two side gears with equal numbers of teeth. Each center gear is attached to each link. The two side gears are coupled with the other side gears of the other bevel gear set with wires. By naming the pan and tilt angle between links 1 and 2 in Fig. 9(b) as θ_p and θ_t , respectively, the proposed coupling mechanism satisfies the following motion:

$$\frac{\theta_p}{2} = \theta_{p1} = \theta_{p2}, \quad \frac{\theta_t}{2} = \theta_{t1} = \theta_{t2} \quad (9)$$

which means that this 2-DOF rolling joint has the same movement as a spherical rolling contact motion.

Fig. 9(c) illustrates an example of the bent pose. Here, we can assign a plane, called a bending plane, where the two center lines of the cylinders of links 1 and 2 coexist. Fig. 9(d) shows the top and side views by projecting the wires to the bending plane. φ and θ , respectively, denote the angle between the panning axis and the bending plane, and the bending angle on the bending frame. As shown in the side view at the bottom part of Fig. 9(d),

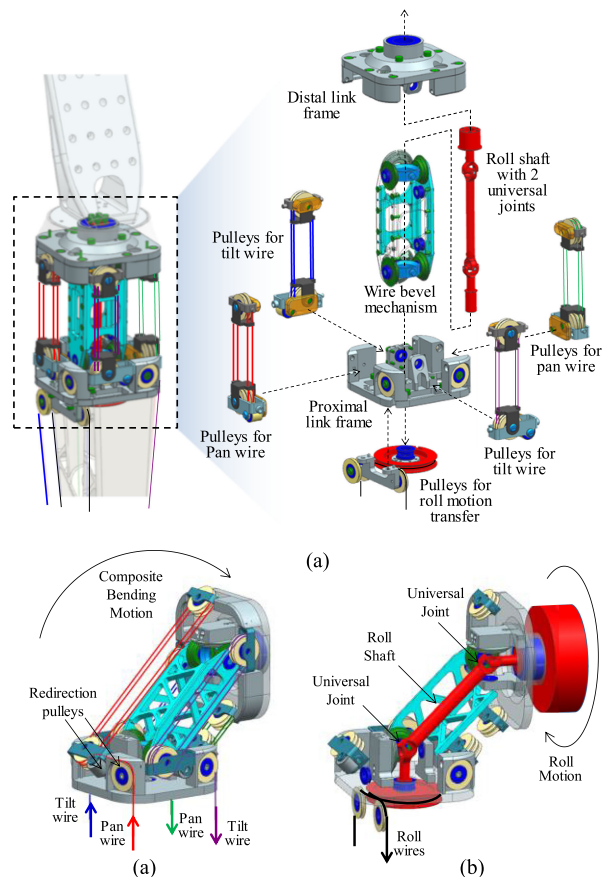


Fig. 10. (a) Detailed design of the 3-DOF wrist and its exploded view. (b) Detailed design of 3-DOF wrist joint. (c) Roll motion transmission mechanism using the shaft with two universal joints.

the configurations of the two wire pairs are similar to the 1-DOF mechanism, except the width between the pulley centers w . The equivalent widths for the pan wire pair and tilt wire pair are $w \sin \varphi$ and $w \cos \varphi$, respectively. Therefore, by substituting w of (7) with $w \cos \varphi$ and $w \sin \varphi$, the relationship between the bending pose (φ, θ) and the motion of wire pair $(\Delta l_p, \Delta l_t)$ can be obtained as

$$\begin{aligned} \Delta l_p &= \Delta l_{P_left} = -\Delta l_{P_right} = nw \sin \varphi \sin \frac{\theta}{2} \\ \Delta l_t &= \Delta l_{T_left} = -\Delta l_{T_right} = nw \cos \varphi \sin \frac{\theta}{2}. \end{aligned} \quad (10)$$

It should be noted that the wire movement of each wire pair is fully symmetrical. This is a very useful property for decreasing the mechanical complexity and simplifying the control algorithm.

Fig. 10(a) presents the detailed design and exploded view of the wrist. The wire bevel mechanism at the center connects the proximal link frame with the distal link frame, causing the 2-DOF rolling motion between the two frames. Four pulley sets for the tension amplification of the pan and tilt wire pairs are attached around the two frames. The extremely short distal link frame is appropriate for large workspace tasks, and the rolling joint mechanism guarantees the nonsingular property

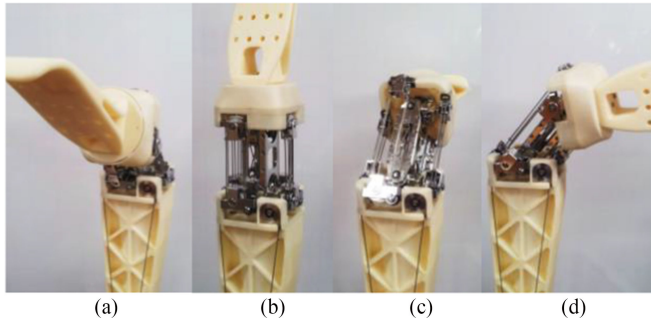


Fig. 11. Implemented wrist joint. (a) Pan 90°. (b) Straight pose. (c) Pan -90°. (d) Tilt 90°.

over the whole workspace. Fig. 10(b) shows the pan and tilt wire paths at a 90° bending pose. To minimize friction, as shown in this figure, the two redirection pulleys for each wire path were used. In general, most robot wrists, as well as those of humans, have 3 DOF for dexterous manipulation. By utilizing the hollow space of the coupling mechanism in Fig. 8(b), the 2-DOF tension-amplification mechanism can be extended to the 3-DOF mechanism. As shown in Fig. 10(a), the roll shaft and two universal joints transfer rotation motion to the distal end of the wrist, thereby enabling the full 3-DOF wrist motion to be achieved. At the bottom of the proximal link frame, there is another pulley set to transfer the roll wire displacement to rotational motion. Fig. 10(c) illustrates the disposition of the wire, pulley, roll shaft, and universal joints at a 90° bending pose.

Fig. 11 shows the implemented 3-DOF wrist. The wrist can bend at $\pm 90^\circ$ and rotate 720°. The wire tension was amplified four times ($n = 4$). To implement the 2-DOF rolling joint with a compact size and minimum backlash, cable-driven bevel gears were used. Six truncated cones with grooves instead of the ordinary bevel gears of Fig. 9(b) were employed. For the coupling motion, four wires were connected from link 1 to link 2 via the truncated cones.

C. Shoulder Actuator Design

For 3-DOF shoulder actuation, back drivable and low backlash joints using capstan drive mechanisms were developed. It is relatively easy to increase the stiffness and strength of the shoulder joints without seriously increasing the rotational inertia because they are at the proximal end. However, to achieve high stiffness with the capstan drive mechanism, several design issues were considered: high payload and stiff steel cables with a large cross-sectional area were used, the total lengths of the cables were made as short as possible, and the driven pulley was designed to have a large diameter because stiffness increases proportionally to the diameter of the driven pulley, even though the cable length increases accordingly.

Fig. 12(a) and Fig. 12(b) illustrates the side and top views of the developed joint mechanism, which has a large hollow shape that is useful for electric wiring and assembling. As shown in the exploded view in Fig. 12(c), a driving pulley and driven pulley wound around by a steel wire construct a capstan drive mechanism. The diameter of the driving pulley and driven pulley are

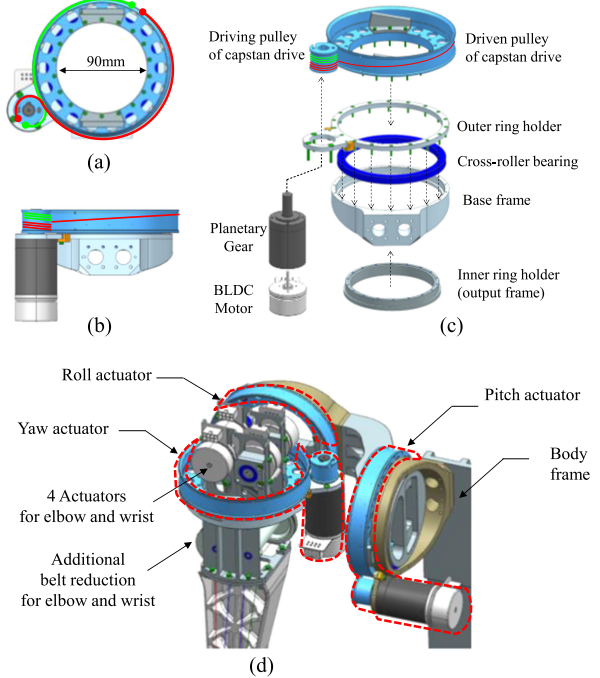


Fig. 12. Detailed design of the shoulder joint mechanism. (a) Top view, (b) front view, and (c) exploded view of the shoulder actuator. (d) 3-DOF shoulder composed of three identical joint mechanisms.

30 and 138 mm, respectively, and the cable length is 530 mm. For additional reduction, a planetary gear was also used. The reduction ratio of the capstan drive and planetary gear were 4.6:1 and 26:1, respectively. Three identical joint mechanisms were combined to implement the 3-DOF shoulder, as shown in Fig. 13(d). The proximal part of the upper arm, which contains heavy components, including wrist and elbow motors, was placed in the hollow space of the yaw joint.

D. Overall Configuration and Wire Routing

As previously mentioned, a human-like configuration with high DOF is crucial for interhuman-level interactions. Furthermore, a proper combination of the proposed mechanisms, without losing the low-inertia property, is also important. Fig. 13(a) shows the configuration of the whole arm (the shoulder joints are simplified). The upper and lower arms have a human-like size of 310 and 336 mm, respectively.

To reduce the rotational inertia, four motors for the elbow and wrist were placed at the proximal end. Each motor has a timing-belt transmission to achieve an additional reduction ratio of 2.57:1 in addition to the reduction by the tension-amplification mechanism. Therefore, the center of mass of the moving part of the whole arm is very close to the body. It is located only 169 mm from the shoulder joint.

Fig. 13(b) illustrates the wire routings of the tension-amplification mechanisms for the elbow and wrist. The red, green, blue, and purple lines denote the wires for the wrist pitch, yaw, roll, and elbow motions, respectively. Because the joints and motors are separated, long wires are required. The lengths of wires for the wrist pitch, yaw, roll joint, and elbow

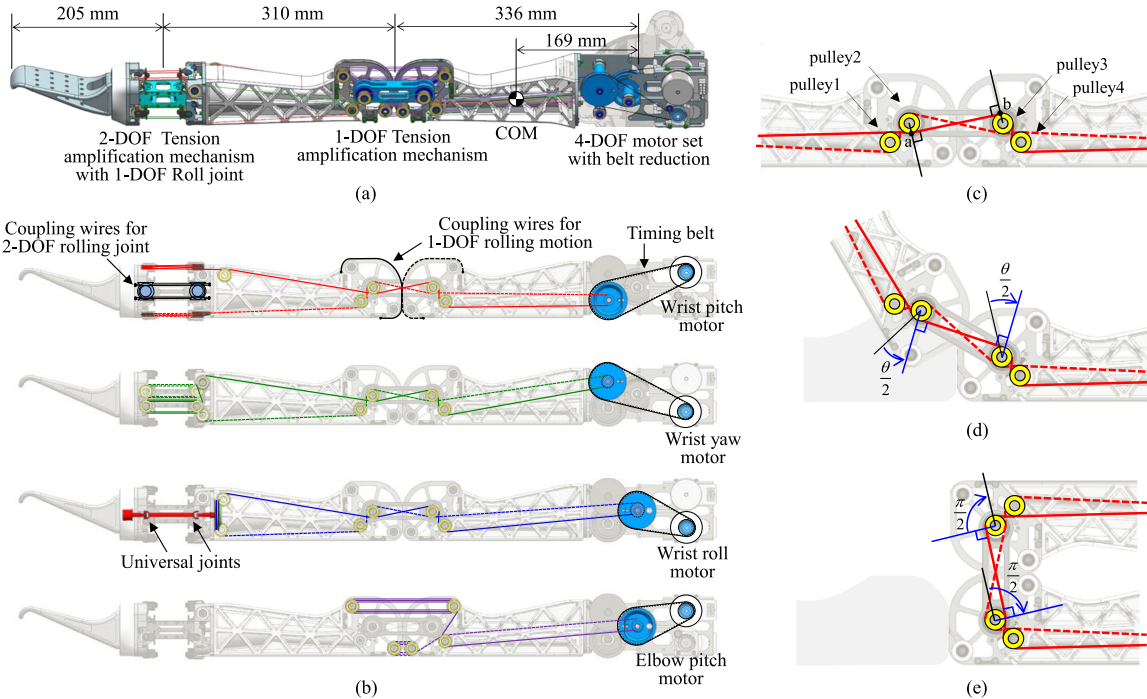


Fig. 13. (a) Proportion of LIMS. (b) Wire routings for wrist pitch (red line), yaw (green line), roll (blue line), and elbow joint (purple line). (c)–(e) Pulley disposition for the decoupling of elbow joint motion and wrist wire movement.

joint are 980, 980, 620, and 1030 mm, respectively (the average lengths of agonistic and antagonistic wire pairs).

The wires for the wrist actuation pass through the elbow joint, and these wire paths can cause the coupling motion with the elbow joint. To decouple the elbow joint motion and wrist wire movement, a pulley disposition on the elbow rolling joint was devised, as shown in Fig. 13(c). There are four idling pulleys, two of which (pulleys 2 and 3) are located at the same axis as the rolling joint. Pulleys 1 and 3 were properly placed to maintain the wire path with a large ROM. The agonistic wire (red solid line) and antagonistic wire (red dotted line) for the wrist actuation were deployed to cross pulleys 2 and 3. The point on the wire departing from pulley 2 (point a in Fig. 13(c)) and the one arriving to pulley 3 (point b in Fig. 13(c)) vary according to the elbow angle.

As shown in Fig. 13(d), assuming that the angle of the elbow joint is θ and the radius of the idle pulley is r_{idle} , the wire length at the departing point increases by $r_{\text{idle}} \cdot \theta/2$ and the length at the arriving point decreases by $r_{\text{idle}} \cdot \theta/2$. Therefore, the length of the wires passing the elbow is not changed at an arbitrary angle of the elbow joint.

Fig. 13(e) shows that the proposed decoupling mechanism works properly until the maximum elbow angle of 180° is reached.

IV. STIFFNESS AND STRENGTH ANALYSIS

In this section, the stiffness and strength of the proposed tension-amplification mechanism are calculated. Here, the joint stiffness and strength caused by the wire stiffness and strength

are considered, and the stiffness and strength of the frames or motors are assumed to be sufficiently high to be treated as rigid bodies. This seems reasonable because the wire is the most dominant flexible component with limited breaking strength in the manipulator. Because ball bearings are used for all pulleys and joints, the friction of the mechanism is also assumed to be negligible.

Let us consider (7) to obtain the tension-torque relationship of the 1-DOF joint. By using the virtual work concept, an energy conservation equation can be obtained as

$$\begin{aligned} \tau_{1\text{DOF}} \delta\theta &= T_{\text{pull}} \delta(\Delta l) - T_{\text{loosen}} \delta(\Delta l) \\ &= \Delta T \delta(\Delta l) \end{aligned} \quad (11)$$

where $\delta(\Delta l)$, $\delta\theta$, and $\tau_{1\text{DOF}}$ denote the infinitesimal changes of the wire motion Δl , that of the bending angle θ , and the resultant joint torque, respectively. ΔT means the difference of the tensions of the pulled wire and loosened wire ($\Delta T = T_{\text{pull}} - T_{\text{loosen}}$). Thus, ΔT equals the force generated by the actuator, as shown in Fig. 6(c) and Fig. 6(d). By differentiating (7), the following equation can be obtained:

$$\frac{\delta(\Delta l)}{\delta\theta} = \frac{nw}{2} \cos \frac{\theta}{2}. \quad (12)$$

By substituting (12) into (11), the relationship between the joint torque $\tau_{1\text{DOF}}$ and the tension difference ΔT can be calculated as

$$\tau_{1\text{DOF}} = \frac{\delta(\Delta l)}{\delta\theta} \Delta T = \left(\frac{nw}{2} \cos \frac{\theta}{2} \right) \Delta T. \quad (13)$$

Considering the maximum torque condition, the pulled wire tension T_{pull} approaches the maximum breaking strength of the wire T_{max} while the loosened wire tension proceeds to 0. Therefore, ΔT equals T_{max} at the maximum torque situation. The maximum torque of the 1-DOF tension-amplification mechanism is obtained as

$$\tau_{1\text{DOF max}} = \left(\frac{nw}{2} \cos \frac{\theta}{2} \right) T_{\text{max}}. \quad (14)$$

This shows that the maximum strength of the joint is proportional to the amplification number n and maximum breaking strength of the wire T_{max} . It decreases as the joint angle θ departs from zero.

The joint stiffness can be derived as follows. Let us assume that the actuator is fixed at a certain angle θ , and the infinitesimal external torque $\delta\tau$ is applied to the joint. Then, the pulled wire will have a higher tension and the loosened wire will have a lower tension as

$$\begin{aligned} T_{\text{pull}} &= k_{\text{wire}}(L_p + \delta(\Delta l)) \\ T_{\text{loosen}} &= k_{\text{wire}}(L_p - \delta(\Delta l)) \end{aligned} \quad (15)$$

where $\delta(\Delta l)$ is an infinitesimal wire movement caused by the external torque. k_{wire} denotes the spring coefficient of each of the wire pairs under the assumption of approximately the same stiffness, and L_p means the preloaded distance of the wires. From (13) and (15), $\delta\tau$ can be calculated as

$$\begin{aligned} \delta\tau &= \left(\frac{nw}{2} \cos \frac{\theta}{2} \right) \Delta T = \left(\frac{nw}{2} \cos \frac{\theta}{2} \right) (T_{\text{pull}} - T_{\text{loosen}}) \\ &= \left(\frac{nw}{2} \cos \frac{\theta}{2} \right) (k_{\text{wire}}(L_p + \delta(\Delta l)) - k_{\text{wire}}(L_p - \delta(\Delta l))) \\ &= \left(\frac{nw}{2} \cos \frac{\theta}{2} \right) 2k_{\text{wire}}\delta(\Delta l). \end{aligned}$$

By canceling $\delta(\Delta l)$ of this equation using (12)

$$\delta\tau = \left(\frac{nw}{2} \cos \frac{\theta}{2} \right) 2k_{\text{wire}} \left(\frac{nw}{2} \cos \frac{\theta}{2} \right) \delta\theta.$$

Consequently, the stiffness of the 1-DOF joint $k_{1\text{DOF}}$ is

$$k_{1\text{DOF}} = \frac{\delta\tau}{\delta\theta} = \left(\frac{n^2 w^2}{2} \cos^2 \frac{\theta}{2} \right) k_{\text{wire}}. \quad (16)$$

This verifies that the joint stiffness is proportional to the square of the amplification number n .

To extend these stiffness and strength properties of the 1-DOF mechanism into that of 2 DOF, we consider the situation of Fig. 9(d). Let us focus on the strength in the banding plane. The maximum joint torque of the 2-DOF mechanism can be calculated by adding the separated contribution of pan wires and tilt wires. If the width between the tilt wire pair $w \cos \varphi$ is greater than the width between the pan wire pair $w \sin \varphi$, the tilt wires reach the maximum breaking strength at the maximum joint torque, while the pan wires contribute only the portion of the width between the pan wires and that of the tilt wires, i.e., $|w \sin \varphi|/|w \cos \varphi|$. Therefore, in this case, which satisfies $|\sin \varphi| < |\cos \varphi|$, the maximum joint torque in total is the sum

of the maximum torque by the tilt wires and the partial torque by the pan wires as

$$\begin{aligned} \tau_{2\text{DOF max}} &= \tau_{\text{max_tilt}} + \frac{|\sin \varphi|}{|\cos \varphi|} \tau_{\text{max_pan}} \\ &= \left(\frac{nw |\cos \varphi|}{2} \cos \frac{\theta}{2} \right) T_{\text{max}} \\ &\quad + \frac{|\sin \varphi|}{|\cos \varphi|} \left(\frac{nw |\sin \varphi|}{2} \cos \frac{\theta}{2} \right) T_{\text{max}} \\ &= \frac{nw}{2} \frac{|\sin^2 \varphi| + |\sin^2 \varphi|}{|\cos \varphi|} \cos \frac{\theta}{2} T_{\text{max}} \\ &= \left(\frac{nw}{2 |\cos \varphi|} \right) \cos \frac{\theta}{2} T_{\text{max}}, \text{ s.t. } |\sin \varphi| < |\cos \varphi| \end{aligned} \quad (17)$$

where $\tau_{\text{max_Tilt}}$ and $\tau_{\text{max_Pan}}$ mean the maximum joint torque due to each wire pair, and these are expanded by substituting w of (14) with $w \cos \varphi$ and $w \sin \varphi$. As we consider the projected situation as Fig. 9(d), the pan wires and the tilt wires have the same bending angle θ . The contribution of the tilt wire is scaled down by $|\sin \varphi|/|\cos \varphi|$ because the tilt wire is not fully stretched to the breaking tension. Similarly, in the case in which the pan wires reach the maximum breaking strength, i.e., $|\sin \varphi| > |\cos \varphi|$, the maximum joint torque is

$$\begin{aligned} \tau_{2\text{DOF max}} &= \frac{|\cos \varphi|}{|\sin \varphi|} \tau_{\text{max_tilt}} + \tau_{\text{max_pan}} \\ &= \left(\frac{nw}{2 |\sin \varphi|} \right) \cos \frac{\theta}{2} T_{\text{max}}, \text{ s.t. } |\cos \varphi| < |\sin \varphi|. \end{aligned} \quad (18)$$

Therefore, combining (17) and (18), the resultant maximum strength is

$$\tau_{2\text{DOF max}} = \left(\frac{nw}{2 \max(|\cos \varphi|, |\sin \varphi|)} \cos \frac{\theta}{2} \right) T_{\text{max}}. \quad (19)$$

This shows that the maximum strength of the joint is proportional to the amplification number n and maximum breaking strength of the wire T_{max} , which is similar to the 1-DOF joint. However, it varies according to the bending direction φ . For instance, if the bending plane coincides with the pan wires or tilt wires ($\varphi = 0, \pm \pi/2$, or π), $\tau_{2\text{DOF max}}$ becomes the same value of the 1-DOF maximum torque $\tau_{1\text{DOF max}}$ in (14). On the other hand, if the bending plane is at the middle of the pan and tilt wires ($\varphi = \pm\pi/4$, or $\pm 3\pi/4$), $\tau_{2\text{DOF max}}$ is $\sqrt{2}$ times higher in strength than $\tau_{1\text{DOF max}}$.

Similarly, the stiffness can be derived as

$$\begin{aligned} k_{2\text{DOF}} &= k_{1\text{DOF_Tilt}} + k_{1\text{DOF_Pan}} \\ &= \left(\frac{n^2 (w \cos \varphi)^2}{2} \cos^2 \frac{\theta}{2} \right) k_{\text{wire}} \\ &\quad + \left(\frac{n^2 (w \sin \varphi)^2}{2} \cos^2 \frac{\theta}{2} \right) k_{\text{wire}} \end{aligned}$$

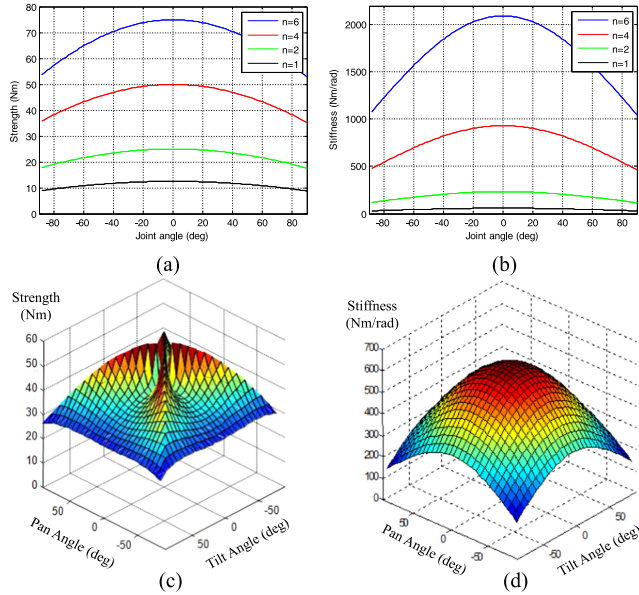


Fig. 14. (a) Strength of the 1-DOF mechanism of the tension-amplification number, $n = 1, 2, 4$, and 6 . (b) Stiffness of the 1-DOF mechanism of $n = 1, 2, 4$, and 6 . (c) Strength of the 2-DOF mechanism ($n = 4$). (d) Stiffness of the 2-DOF mechanism ($n = 4$).

where $k_{1\text{DOF,Tilt}}$ and $k_{1\text{DOF,Pan}}$ denote the stiffness on account of the tilt wire and pen wire pairs, respectively. These were expanded by substituting w of (16) with $w \cos \varphi$ and $w \sin \varphi$. Consequently, the stiffness of the 2-DOF joint $k_{2\text{DOF}}$ is

$$k_{2\text{DOF}} = \left(\frac{n^2 w^2}{2} \cos^2 \frac{\theta}{2} \right) k_{\text{wire}}. \quad (20)$$

It is notable that the stiffness of the 2-DOF joint is not affected by the bending direction φ , which means that the wrist has the same stiffness regardless of the bending direction. Fig. 14 illustrates the stiffness and strength changes of the 1-DOF and 2-DOF tension-amplification mechanisms obtained from (14), (16), (19), and (20). As shown in Fig. 14(a) and Fig. 14(b), the joint has maximum strength and stiffness at the straight pose. Fig. 14(b) shows that the stiffness with tension amplification $n = 6$ (blue line) is 36 times higher than the stiffness of $n = 1$ (black line). As previously mentioned, the strength of the 2-DOF joint has different values according to the bending direction, as shown in Fig. 14(c). Meanwhile, the stiffness always has the same value regardless of the bending direction, which is evident from the point symmetrical shape of the graph in Fig. 14(d).

Please note that the strength mentioned in this section is the maximum strength derived from the wire breaking strength. Thus, the actual maximum strength, or payload, should be determined by considering this strength as well as the maximum motor torque and motor driver performance.

V. IMPLEMENTATION AND PERFORMANCE VALIDATION

Fig. 15(a) shows the implemented manipulator, LIMS. The upper arm and forearm frames were fabricated from ABS material using a 3-D printer (FORTUS 360MC, Stratasys). A dummy hand, which was also fabricated by the 3-D printer, was mounted

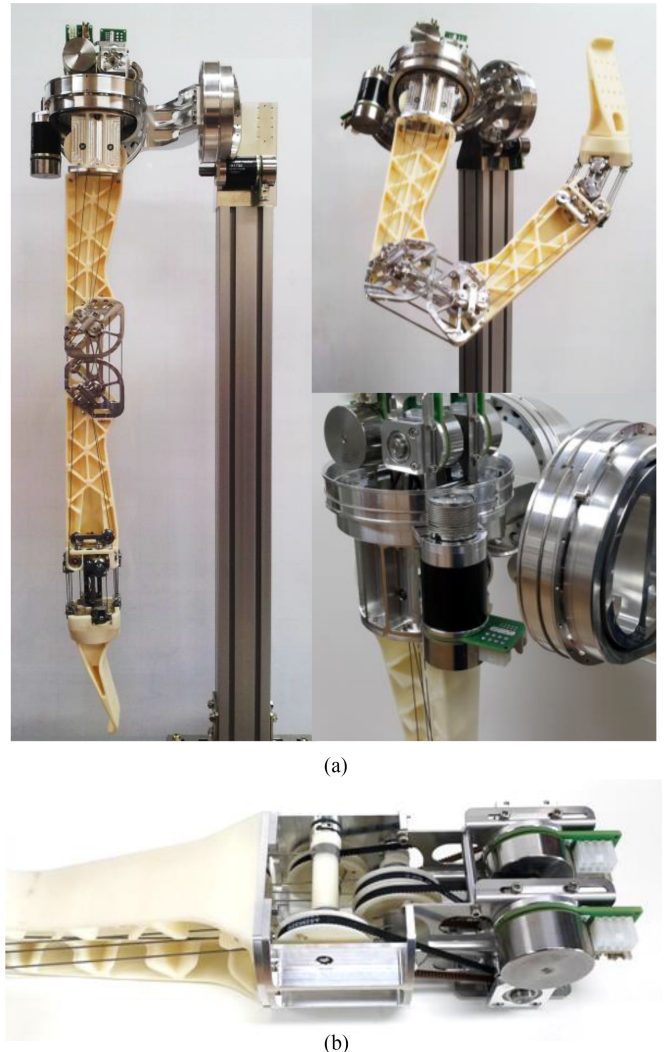


Fig. 15. (a) Implemented robot LIMS. (b) Motor and pulley reduction assembly for wrist and elbow actuation.

at the end of the wrist. Most of the other components were machined using aluminum alloy (AL6061-T6). For the capstan drive mechanism of the shoulder, steel wires with diameters of 1.59 mm (7 × 19 construction and breaking strength of 1197 N) were used. In addition, 70-W MAXON EC45 motors with two-stage planetary gears were used to drive the capstan drive mechanism.

As shown in Fig. 15(b), at the proximal end of the upper arm, three 50-W MAXON EC45 motors and one 70-W MAXON EC45 motor without gear heads were mounted for actuation of the 3-DOF wrist and 1-DOF elbow. These motors were chosen on account of their higher torque than other line ups. Nevertheless, they have the drawback of rotor inertia that is several to ten times higher than that of others with similar specifications.

Four MAXON EPOS2 24/5 motor drivers for the shoulder and elbow, as well as three MAXON POS2 24/2 drivers for the wrist, were used. They were all mounted at the body frame. The 5-mm-wide timing belts composed of polyurethane rubber and aramid fiber were used to produce the additional reduction of the

TABLE I
DESIGN PARAMETERS

Items	Design Parameters	
	1-DOF Elbow	2-DOF Wrist Pan and Tilt
n	6	4
w	80 mm	67 mm
k_{wire}	18.17 N/mm	19.10 N/mm
T_{\max}	312 N	312 N

TABLE II
MASS–INERTIA COMPARISON

	Items	LIMS	Human
<i>Mass (kg)</i>	upper arm	1.28	2.5
	lower arm	0.64	1.45
	dummy hand	0.32	0.53
	shoulder	3.60	–
<i>Link inertia ($\text{kg}\cdot\text{mm}^2$)</i>	upper arm	18 796	14 845
	lower arm	6895	9355
	hand ¹⁾	694	1370
<i>Reflected rotor inertia ($\text{kg}\cdot\text{mm}^2$)</i>	shoulder	193 444	–
	elbow	108 732	–
	wrist	33 896	–
<i>Inertia with distal links²⁾ ($\text{kg}\cdot\text{mm}^2$)</i>	shoulder to hand	405 323	639 651
	elbow to hand	86 204	139 487
	wrist to hand	5694	9651

¹⁾ Dummy hand with the distal part of the wrist mechanism.

²⁾ Straight pose. Reflected motor inertia is not included.

wrist and elbow joint. For the tension-amplification mechanism, nylon-coated steel wires with diameters, including the coating, of 0.762 mm (7 × 19 construction and a breaking strength of 312 N) were used.

The stiffness per unit length of this wire was 18 720 N. Identical pulleys with diameters of 16 mm were used for the tension-amplification mechanisms and the decoupling mechanism at the elbow. To minimize this frictional loss, the manipulator does not rely on any frictional components such as Bowden cables and only pulleys with bearings were used for wire routing. For the routing of the wrist pan and tilt wires, a total of nine pulleys were used. For the wrist roll and elbow wire routing, four and seven pulleys were used, respectively. The design parameters relating to the tension-amplification mechanisms of LIMS are given in Table I.

A. Inertia and Effective Mass

Table II compares the mass and inertia properties of the developed manipulator with that of a human [25]. The mass beyond the shoulder of LIMS is 2.24 kg, which is lighter than that of the human of 4.48 kg. The rotational inertia of the shoulder of LIMS, including whole distal link, is 405 323 $\text{kg}\cdot\text{mm}^2$, which is also lighter than that of the human of 639 651 $\text{kg}\cdot\text{mm}^2$. However, if the reflected rotor inertia of the motor and reduction pulley is taken into account, the shoulder inertia of LIMS is 598 767 $\text{kg}\cdot\text{mm}^2$, which is comparable to that of a human. The elbow and wrist inertias of LIMS are substantially higher than those of a human. The rotor inertia does not aggravate the safety

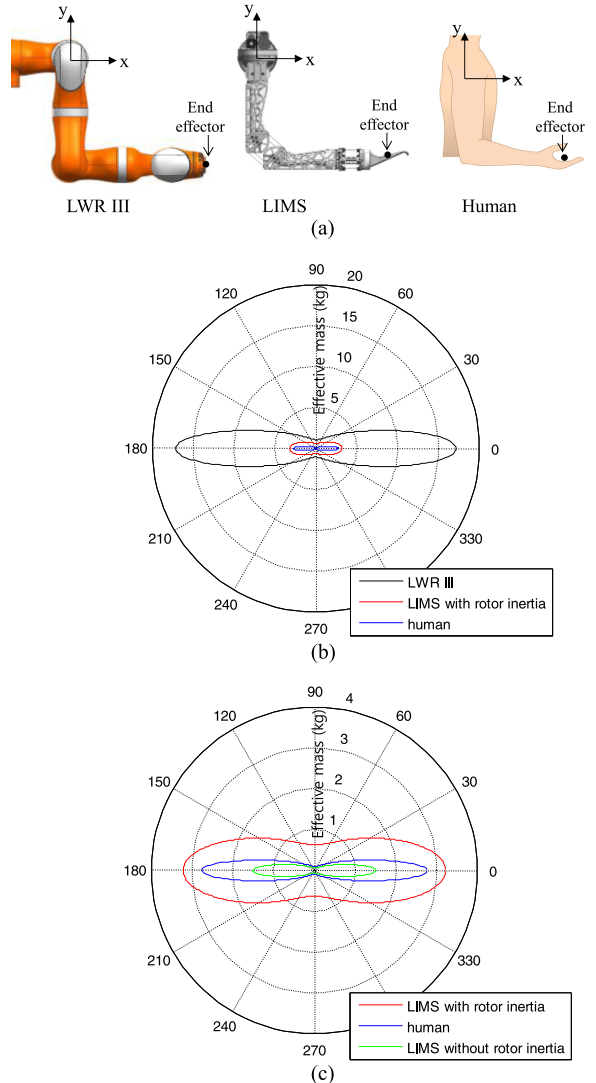


Fig. 16. (a) Configuration for effective mass calculation. (b) Effective mass. (c) Closed-up diagram of the effective mass.

owing to the compliance between the links and motors, as mentioned in Section II. However, the high reflected rotor inertia can cause an undesirable sensation during the interaction. This means that further improvement is possible by replacing the proper motors with low rotor inertia.

To compare the effect of mass and inertia in the workspace, the effective masses of LWR III, LIMS, and a human arm were calculated [26]. The configuration of the shoulder, elbow, and wrist joints was set to -90° , 90° , and 0° , respectively, as shown in Fig. 16(a). As evident in Fig. 16(b), the effective masses of LWR III, a human arm, and LIMS are 17.1, 2.76, and 3.22 kg, respectively. This proves that the effective mass of LIMS is significantly lower than that of other lightweight manipulators and that an effective mass similar to that of a human arm is achievable by using the proposed mechanism.

Note that the effective mass of LIMS in Fig. 16(b) includes reflected rotor inertia. If we consider safety, the effective mass without the rotor inertia can be considered. LIMS has 1.51-kg effective mass, as shown in Fig. 13(c), which is

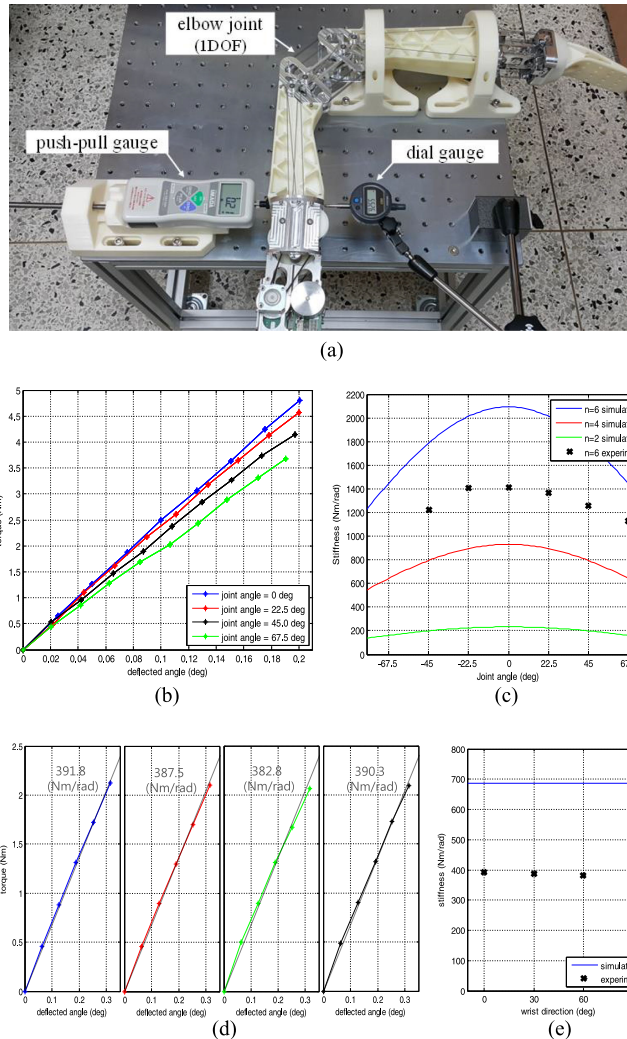


Fig. 17. (a) Experimental setup for stiffness measurement. (b) Angle–torque graphs of the elbow at 0°, 22.5°, 45°, and 67.5°. (c) Comparison of measured and simulated elbow stiffness. (d) Angle–torque graphs of the wrist at various bending directions (blue, red, green, and black denote 0°, 30°, 60°, and 90°, respectively). (e) Comparison of measured and simulated wrist stiffness.

exceedingly smaller than in humans. This implies that LIMS has the potential to be safer than a human arm.

B. Joint Stiffness

To verify the amplified stiffness property of the proposed mechanism, the stiffness of the elbow and wrist joints was measured. Fig. 17(a) shows the experimental setup. The force and displacement were measured by using a push–pull gauge (I-DS2-50N, 1-g·f resolution, maximum force 50 N, Imada Co.) and an absolute digimatic indicator (ID-S112SB, 0.001-mm resolution, Mitutoyo Co.). Fig. 17(b) illustrates the measured angle–torque relationship at several elbow angles.

To compare the measured stiffness with the theoretical values of (16), the measured stiffness is plotted in Fig. 14(b). The black cross points in Fig. 17(c) denote the measured stiffness at the elbow angles of −45°, −22.5°, 0°, 22.5°, and 45°. The measured stiffness at 0° is 1410 N·m/rad, which is smaller than the

TABLE III
SPECIFICATIONS RELATING TO STIFFNESS AND STRENGTH

Items	Specifications	
Stiffness ¹⁾	elbow	Simulation: 2093 N·m/rad Experiment: 1410 N·m/rad
	wrist	Simulation: 685 N·m/rad Experiment: 388 N·m/rad
Max torque ¹⁾	shoulder	peak 71.9 N·m, cont. 16.6 N·m
	elbow	peak 48.8 N·m, cont. 11.2 N·m
	wrist	peak 12.5 N·m, cont. 4.1 N·m
Equivalent gear ratio ¹⁾	shoulder	119.6:1
	elbow	88.2:1
	wrist	49.2:1

¹⁾ Calculated or measured values at the straight pose (bending angle = 0°).

calculated stiffness 2093 N·m/rad. This difference is considered to come from the frame flexibility and the elasticity of the extra wires in the actuators. Especially, the 3-D-printed ABS links can cause substantial compliance.

This stiffness is approximately seven times smaller than 10 000 N·m/rad of LWR III, which uses conventional harmonic drive gears. However, considering the stiffness–inertia ratio from (3), LIMS has 7233 m/rad, while LWR III has a similar value of 8333 m/rad (inertia of LWR III from the elbow to the wrist is considered as approximately 1.2 kg·m²). This means that the control performance of LIMS is expected to be comparable to LWR III. The stiffness–inertia ratio of the human elbow is 2509 m/rad (stiffness 250 N·m/rad and inertia 0.139 kg·m²). This shows that LIMS has the property of industrial robots rather than a human with respect to the control performance.

The wrist stiffness was measured in a similar way. Fig. 17(d) illustrates the measured stiffness in a straight pose around various bending directions of 0°, 30°, 60°, and 90°. As proved in (20), the stiffness is not related to the bending direction. The cross dots in Fig. 17(e) represent the measured wrist stiffness. They verify that the stiffness has almost the same value regardless of the bending direction. The average stiffness is 388 N·m/rad, which is smaller than the theoretical value 685 N·m/rad. It is also believed that this difference is caused by the flexible frame and extra wires. In addition, the wire bevel mechanism to emulate spherical rolling contact produces substantial compliance.

Table III summarizes the specifications relating to stiffness and strength. The maximum torque due to the wire breaking strength obtained by (14) is always higher than the maximum torque produced by the motors and drivers. Therefore, the strength data in the table show the maximum torque limited by the motor and driver performance.

To evaluate the overall arm deformation for different loads, a payload experiment was conducted. The configuration was set to the pose shown in Fig. 16(a). The load was applied at the point 102.5 mm inside from the tip of the hand and the motions were recorded by a motion tracker (PST-Iris, Polaris Co.). Fig. 18 shows snapshots of the deformation and downward displacement for three different loads of 1, 2, and 3 kg. As shown in Fig. 18(b), the maximum displacement was 18.6 mm

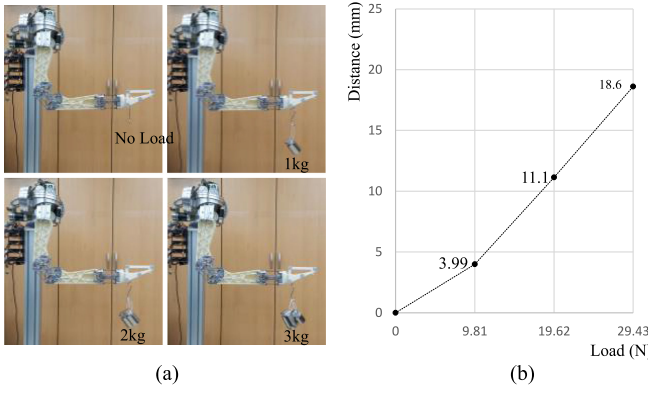


Fig. 18. (a) Payload tests for loads of 1, 2, and 3 kg. (b) Deflections for each load.

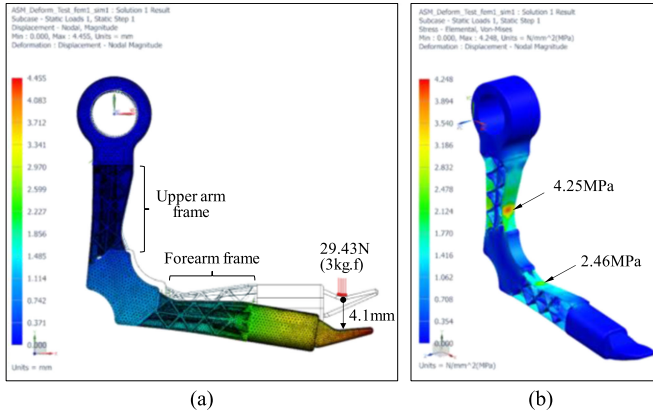


Fig. 19. (a) Deformation of the ABS frames by a 39.24-N load (the deformation is exaggerated). (b) Maximum stress on the fore arm and upper arm frames.

at 29.43 N (3 kgf) which is the maximum payload of LIMS. This deformation is thought to be the effect of both the joint compliance due to the cable elasticity (explained in Section IV) and the compliance of the frame and other components such as bearings for joints.

As previously mentioned, frames made from ABS material can cause substantial compliance. To estimate this frame compliance, a finite-element method simulation was carried out using NX Nastran (SEIMENS Co). All parts except for the forearm and upper arm frames were replaced by dummy parts with sufficiently high strength and stiffness to simulate the frame deformation only. Fig. 19(a) shows that the deformation of the frames and downward displacement of the position with the maximum load of 29.43 N was 4.1 mm. As shown in Fig. 19(b), the maximum stress on the frames for a 29.43-N load is 4.25 MPa, which is a sufficiently low value compared with the maximum stress of the 3-D-printed ABS material (33 MPa). To achieve higher stiffness, other materials can be used. For instance, if aluminum alloy AL6061 is used, the stiffness will be about 30 times higher, but the weight becomes 2.3 times heavier. If carbon fiber reinforced plastic is used, the stiffness would be high, similar to AL6061, and the weight would be only about 30% higher than that of the ABS frames, but this material is difficult to fabricate and high in cost. In contrast, the stiffness can be

TABLE IV
MEASURED FRICTIONAL TORQUE OF THE ELBOW AND WRIST

Joints	Direction	Friictional Torque
Elbow	Flexion	0.93 Nm
	Extension	0.90 Nm
Wrist Pan	Radial motion	0.76 Nm
	Ulnar motion	0.69 Nm
Wrist Tilt	Flexion	0.88 Nm
	Extension	0.92 Nm
Wrist Roll	Pronation	0.073 Nm
	Supination	0.072 Nm

The diagram illustrates the joints and their degrees of freedom: Elbow Flexion/Extension, Wrist Pan (Radial/Ulnar motion), Wrist Tilt (Flexion/Extension), and Wrist Roll (Pronation/Supination).

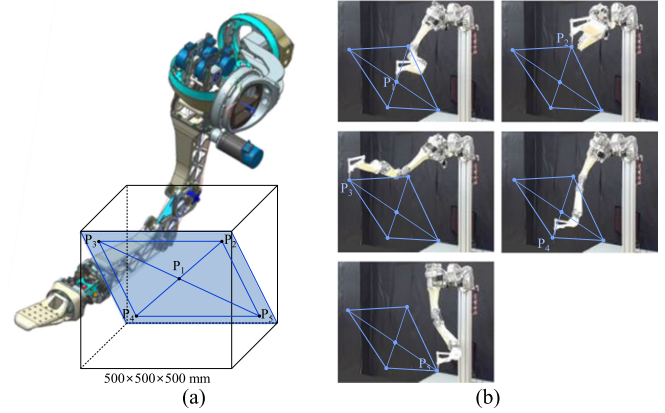


Fig. 20. Repeatability test based on ISO 9283:1998. (a) Test plane (blue diagonal rectangle) and five test poses (P₁, P₂, P₃, P₄, and P₅). (b) Snapshots of the robot pose at the test points.

increased by modifying the frame design to have a thick and sturdy shape.

C. Friction and Back-Drivability

Back-drivability can be evaluated by the three output-side terms: inertia, damping, and friction. The inertia has already been discussed in Section V-A. In particular, friction can be the dominant loss that degrades the back-drivability. The frictional torques of the elbow and wrist joint were measured by experiment. The experimental setup is similar to the stiffness experiment in Fig. 17(a), but all motors were turned off to measure the friction of the joints. The push-pull gauge slowly pushed the frame five times. The average forces were obtained and the corresponding frictional torques were calculated.

Table IV shows the measured frictional torques, which are substantially low. This result verifies that in practice the frictional torque is negligible compared to the joint output torque.

D. Repeatability

Repeatability is one important factor of the performance of the manipulators. A repeatability test was conducted according to the ISO 9283 performance criteria and related test method [28]. As illustrated in Fig. 20(a), a cube of size 500 x 500 x 500 mm was placed in the workspace of LIMS and the diagonal plane inside the cube was defined as a test plane (blue rectangle

TABLE V
POSITIONING REPEATABILITY TEST RESULTS

Pose	MEAN (MM)	STD. DEV. (MM)	3-SIGMA (MM)
P ₁	0.138	0.066	0.335
P ₂	0.148	0.074	0.369
P ₃	0.103	0.048	0.247
P ₄	0.187	0.113	0.528
P ₅	0.189	0.116	0.536
Total	0.153	0.091	0.426

in Fig. 20(a)). Point P₁ was set to the center of the test plane and other four points were placed at four corners of a rectangle, which has 80% of the length of the sides of the test plane. The orientation at each point was set so that the hand would aim in the front direction. The robot successively moved to the poses P₁, P₂, P₃, P₄, and P₅ and repeated this path 30 times. The position and orientation of the hand were recorded by the PST-Iris motion tracker. Fig. 20(b) shows snapshots of the robot pose at each point.

To calculate the repeatability, the mean position of each pose was calculated and then the average distance, its standard deviation, and 3-sigma distance between the mean and recorded positions were obtained. These are summarized in Table V. The 3-sigma distance, which corresponds to the positioning repeatability of ISO 9283, is 0.425 mm. This is reasonably small for most human-like tasks but it is higher than that of industrial robots. For instance, the positioning repeatability of Kuka's iiwa, according to ISO 9283, is 0.1 mm.

E. Combined Motion Test and Preliminary High-Speed Interaction Test

To validate the control and interaction performance, high-speed motion tests using the whole arm were conducted. The manipulator repeatedly moved between pose A and pose B, as shown in Fig. 21(a). Each joint of the manipulator was controlled by PID position controllers and followed a predefined minimum acceleration trajectory in joint space. Three motions were established to have the same path and different speeds, where the end-effector speeds were to be more than 1, 3, and 5 m/s for motion 1, motion 2, and motion 3, respectively. The hand and link motions in 3-D space were recorded by the motion tracker PST-Iris.

Fig. 21(b) illustrates the paths of the end effector of the three motions. Motions 1, 2, and 3 are denoted by black, blue, and red curves, respectively, and they have the maximum speed of 1.04, 3.21, and 5.35 m/s. Owing to the extremely low arm inertia, the manipulator can easily gain high speed using only a small portion of the motor power capacity. As shown in the bottom right graph of Fig. 21(b), the three motions accurately reach poses A and B. However, on account of the delicate difference of the motor driver timing and frame deformation at high speed, the paths between the two target poses do not coincide.

Fig. 21(c) shows the distance and speed graphs of motion 3. The average distance of the trajectory is 2.93 m

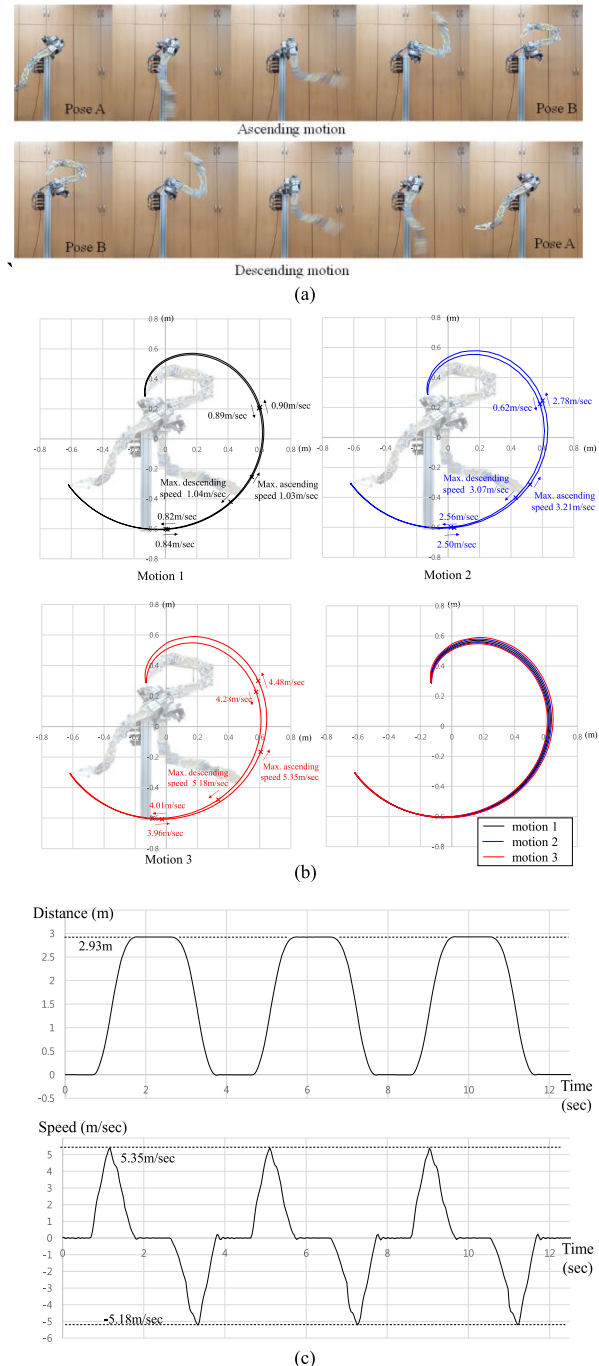


Fig. 21. High-speed motion test. (a) Snapshots of the test motion. (b) End-effector paths of three different speed profiles. (c) Distance and speed graphs of motion 3.

and the end effector has maximum and minimum speeds of 5.35 and 5.18 m/s when ascending and descending, respectively.

To estimate the potential capability of high-speed human-robot interaction using LIMS, a preliminary interaction test was conducted. During the ascending motion of motion 3, a subject interrupted the robot using one hand near the point of maximum speed. To prevent potential abrasion of the human hand, 8-mm rubber sheet was attached to the dummy hand. The only

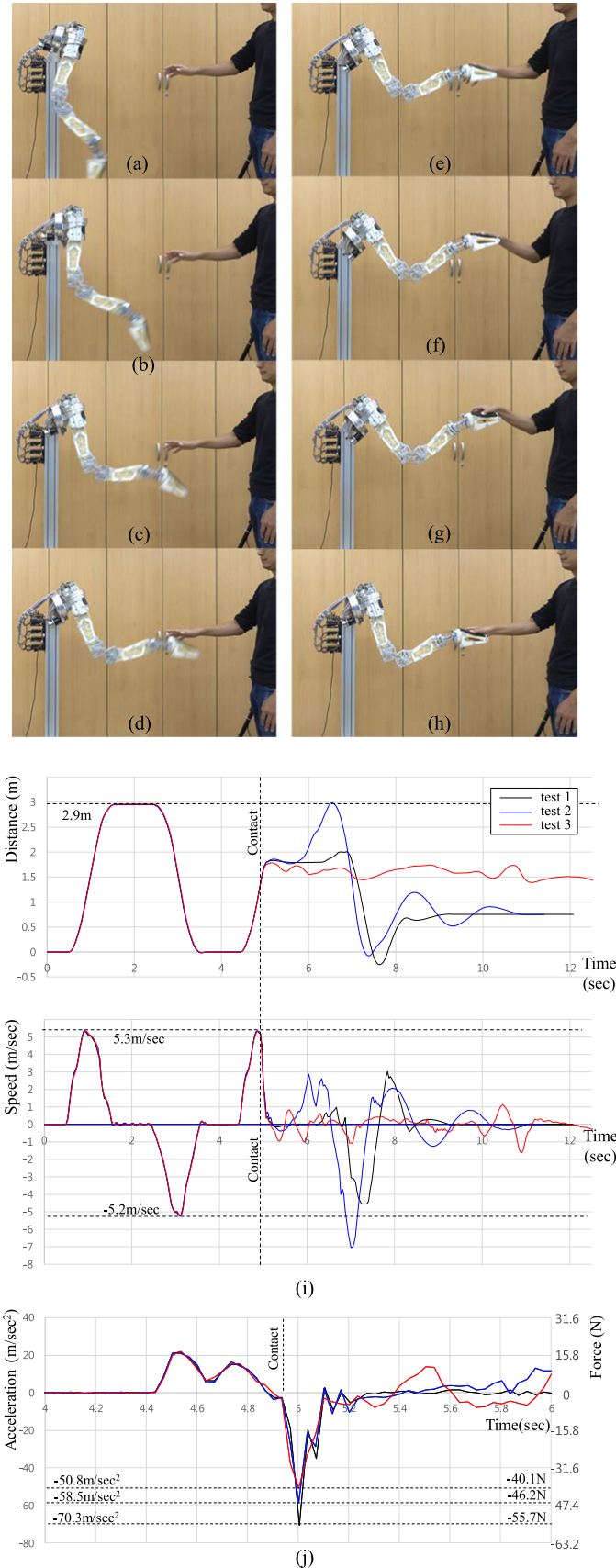


Fig. 22. Preliminary high-speed interaction test. (a)–(h) Snapshots of the high-speed interaction test. (i) Distance and speed results for the three tests. (j) Acceleration and force results.

safety algorithm was the joint torque limit with no other safety algorithm, such as disturbance observers.

Fig. 22(a) to (h) presents images of the experiment. Contact occurred in a short period between (d) and (e). Fig. 22(i) presents the distance and speed graphs of three different test results. As shown in the speed graphs, the contact occurs at more than 5 m/s, which can be a very dangerous speed for conventional industrial robots. However, the manipulator rapidly decelerated owing to the low effective mass, and the human hand received minimal force and energy without incurring harm or an uncomfortable sensation. Fig. 22(j) shows the acceleration for the three different tests near contact time (4–6 s). Right after contact, the deceleration approached the minimum values –70.5, –58.5, and –50.8 m/s² for tests 1–3, respectively. If we know the effective mass of LIMS in the direction of the contact, the maximum force applied to the human hand can be estimated by multiplying the effective mass and the magnitudes of these deceleration values. In Fig. 16(c), the effective mass of LIMS with rotor inertia at an angle of 60° is 0.790 kg. Therefore, the estimated maximum forces are 55.7, 46.2, and 40.1 N, respectively.

To measure the actual interaction force, another high-payload push-pull gauge (I-DS2-500N, 10-gf resolution, maximum force 500 N, Imada Co.) was positioned by the human hand and the peak force was measured. Five tests were conducted, and the peak forces were 56.8, 65.7, 52.1, 54.3, and 60.7 N. These are higher than the forces estimated from the deceleration values. The reason for this could be that the actual force arises from the estimated inertial force as well as the force caused by the motor torque. Moreover, the mass of the hand holding the push-pull gauge is larger than that of a bare hand. These force estimations and actual force measurements verify that the impact is adequately regulated to a low value, even at high speed, owing to the extremely low inertia.

VI. CONCLUSION AND FUTURE WORK

In this paper, a unique manipulator with low mass and inertia that does not lose stiffness or strength performance is presented. It is basically a cable-driven manipulator. However, by utilizing a novel lightweight tension-amplification mechanism, the manipulator maintains high stiffness and strength. Especially, the joint stiffness, which is highly related to the motion control performance, is amplified by a quadratic order. 1-DOF and 3-DOF joint mechanisms with the tension-amplification mechanism were herein presented. They were combined to develop a 7-DOF anthropomorphic manipulator named LIMS. The mass and inertia beyond the shoulder were 2.24 kg and 0.599 kg·m², respectively, which were lower than those of a human. Owing to the proposed tension-amplification mechanism, the manipulator has high joint stiffness compared to the inertia. For instance, the elbow has a stiffness of 1410 N·m/rad, which is approximately seven times higher than that of humans. Considering the ratio of the stiffness to inertia, it is expected to possess control performance that is comparable to that of conventional industrial manipulators. Comprehensive experiments were conducted that included joint stiffness tests and high-speed interaction tests to verify the feasibility of the developed manipulator. The results

show that the proposed manipulator can surpass the limits of conventional manipulators by achieving safety similar to that of human arms while maintaining some of the performance of industrial manipulators. However, owing to the lightweight ABS frames and cable-driven remote actuation, LIMS has relatively higher compliance and lower repeatability than industrial robots, which was verified by the experiments. To improve the frame compliance, a light material with high stiffness and strength such as carbon-reinforced engineering plastic can be used. High-payload cross-roller bearings could also be used to increase the joint stiffness and strength.

In future research, in addition to these improvements, optimizations and progress with the mechanism, such as optimizing the weight distribution, adding an impact-proof mechanism to reduce damage of the robot, and replacing motors for lower rotor inertia, will be conducted. Safety tests for unconstrained and constrained impacts will also be performed. A thorough investigation of human behavior during high-speed interaction, and the adoption of this investigation to human–robot interaction, is another key research goal.

REFERENCES

- [1] R. Bischoff *et al.*, “The KUKA-DLR lightweight robot arm—A new reference platform for robotics research and manufacturing,” in *Proc. 6th Ger. Conf. Robot.*, Jun. 2010, pp. 1–8.
- [2] M. Laffranchi, N. Tsagarakis, and D. Caldwell, “Safe human robot interaction via energy regulation control,” in *Proc. IEEE/RSJ Int. Conf. Intell. Robots Syst.*, 2009, pp. 35–41.
- [3] G. A. Pratt and M. M. Williamson, “Series elastic actuators,” in *Proc. IEEE/RSJ Int. Conf. Intell. Robots Syst.*, 1995, vol. 1, pp. 399–406.
- [4] A. Bicchi and G. Tonietti, “Fast and soft-arm tactics,” *IEEE Robot. Autom. Mag.*, vol. 11, no. 2, pp. 22–33, Jun. 2004.
- [5] H. Vallery, J. Veneman, E. Asseldonk, R. Ekkelenkamp, M. Buss, and H. D. Kooij, “Compliant actuation of rehabilitation robots,” *IEEE Robot. Autom. Mag.*, vol. 15, no. 3, pp. 60–69, Sep. 2008.
- [6] G. Mathijssen, D. Lefeber, and B. Vanderborght, “Variable recruitment of parallel elastic elements: Series–parallel elastic actuators (SPEA) with dephased mutilated gears,” *IEEE/ASME Trans. Mechatronics*, vol. 20, no. 2, pp. 594–602, Apr. 2015.
- [7] C.-M. Chew, G.-S. Hong, and W. Zhou, “Series damper actuator: A novel force/torque control actuator,” in *Proc. IEEE/RAS Int. Conf. Humanoid Robots*, 2004, vol. 2, pp. 533–54.
- [8] S. Wolf, O. Eiberger, and G. Hirzinger, “The DLR FSJ: Energy based design of a variable stiffness joint,” in *Proc. IEEE Int. Conf. Robot. Autom.*, 2011, pp. 5082–5089.
- [9] F. Petit, W. Friedl, H. H'opner, and M. Grebenstein, “Analysis and synthesis of the bidirectional, antagonistic variable stiffness mechanism,” *IEEE/ASME Trans. Mechatronics*, vol. 20, no. 2, pp. 684–695, Apr. 2015.
- [10] A. Jafari, N. G. Tsagarakis, and D. G. Caldwell, “A novel intrinsically energy efficient actuator with adjustable stiffness (AwAS),” *IEEE/ASME Trans. Mechatronics*, vol. 18, no. 1, pp. 355–365, Feb. 2013.
- [11] J. Choi, S. Hong, W. Lee, S. Kang, and M. Kim, “A robot joint with variable stiffness using leaf springs,” *IEEE Trans. Robot.*, vol. 27, no. 2, pp. 229–238, Apr. 2011.
- [12] T. Lens and O. von Stryk, “Investigation of safety in human–robot interaction for a series elastic, tendon-driven robot arm,” in *Proc. IEEE/RSJ Int. Conf. Intell. Robots Syst.*, 2012, pp. 4309–4314.
- [13] Y.-J. Kim, J. Kim, J.-W. Lee, K.-M. Park, K.-S. Roh, and J.-Y. Choi, “RoboRay hand: A highly backdrivable robotic hand with sensorless contact force measurements,” in *Proc. IEEE Int. Conf. Robot. Autom.*, 2014, pp. 6712–6718.
- [14] K. Salisbury, W. Townsend, B. Eberman, and D. DiPietro, “Preliminary design of a whole-arm manipulation system (WAMS),” in *Proc. IEEE Int. Conf. Robot. Autom.*, Philadelphia, PA, USA, 1988, pp. 254–260.
- [15] 2017. [Online]. Available: <http://www.barrett.com/products-arm-specifications.htm>
- [16] J.-J. Park and J.-B. Song, “Safe joint mechanism using inclined link with springs for collision safety and positioning accuracy of a robot arm,” in *Proc. IEEE Int. Conf. Robot. Autom.*, 2010, pp. 813–818.
- [17] C. Cho and S. Kang, “Design of a static balancing mechanism for a serial manipulator with an unconstrained joint space using one-DOF gravity compensators,” *IEEE Trans. Robot.*, vol. 30, no. 2, pp. 421–431, Apr. 2014.
- [18] A. S. Shafer and M. R. Kermani, “On the feasibility and suitability of MR fluid clutches in human-friendly manipulators,” *IEEE Trans. Mechatronics*, vol. 16, no. 6, pp. 1073–1082, Dec. 2011.
- [19] P. Yadmellat, A. S. Shafer, and M. R. Kermani, “Design and development of a single-motor, two-DOF, safe manipulator,” *IEEE Trans. Mechatronics*, vol. 19, no. 4, pp. 1384–139, Aug. 2014.
- [20] M. Zinn, O. Khatib, B. Roth, and J. K. Salisbury, “Playing it safe,” *IEEE Robot. Autom. Mag.*, vol. 11, no. 2, pp. 12–21, Jun. 2004.
- [21] Y.-J. Kim, “Design of low inertia manipulator with high stiffness and strength using tension amplifying mechanisms,” in *Proc. IEEE/RSJ Int. Conf. Intell. Robots Syst.*, 2015, pp. 5850–5856.
- [22] S. Haddadin, A. Albu-Schäffer, and G. Hirzinger, “Requirements for safe robots: Measurements, analysis and new insights,” *Int. J. Robot. Res.*, vol. 28, no. 11, pp. 1507–1527, Nov. 2009.
- [23] K. P. Tee, E. Burdet, C. M. Chew, and T. E. Milner, “A model of force and impedance in human arm movements,” *Biol. Cybern.*, vol. 50, no. 5, pp. 368–375, May 2004.
- [24] J. Lee *et al.*, “Tension propagation analysis of novel robotized surgical platform for transumbilical single-port access surgery,” in *Proc. IEEE/RSJ Int. Conf. Intell. Robots Syst.*, 2013, pp. 3083–3089.
- [25] “Man-Systems Integration Standards.” 1995. [Online]. Available: <http://msis.jsc.nasa.gov/sections/section03.htm>
- [26] O. Khatib, “Inertial properties in robotic manipulation: An object-level framework,” *Int. J. Robot. Res.*, vol. 14, no. 1, pp. 19–36, 1995.
- [27] M. Zinn, B. Roth, O. Khatib, and J. Salisbury, “A new actuation approach for human friendly robot design,” *Int. J. Robot. Res.*, vol. 23, nos. 4/5, pp. 379–398, 2004.
- [28] “ISO 9283:1998, Manipulating industrial robots—Performance criteria and related test methods.” *Int. Org. Standardization*. 1998. [Online]. Available: <https://www.iso.org/standard/22244.html>



Yong-Jae Kim received the M.S. and Ph.D. degrees in electrical engineering and computer science from Korea Advanced Institute of Science and Technology, Daejeon, South Korea, in 1998 and 2003, respectively.

He was a Research Staff Member with Samsung Advanced Institute of Technology, South Korea. He is currently an Assistant Professor with Korea University of Technology and Education, Cheonan, South Korea. His research interests include electromechanical design and control of safe manipulators, bioinspired robotic hands, soft-wearable robots, surgical robots, and humanoid robots for physical human–machine interaction.